

Atomic-Scale Observation of Electrochemically Reversible Phase Transformations in SnSe₂ Single Crystals

Sungkyu Kim, Zhenpeng Yao, Jin-Myoung Lim, Mark C. Hersam, Chris Wolverton, Vinayak P. Dravid,* and Kai He*

2D materials have shown great promise to advance next-generation lithium-ion battery technology. Specifically, tin-based chalcogenides have attracted widespread attention because lithium insertion can introduce phase transformations via three types of reactions—intercalation, conversion, and alloying—but the corresponding structural changes throughout these processes, and whether they are reversible, are not fully understood. Here, the first real-time and atomic-scale observation of reversible phase transformations is reported during the lithiation and delithiation of SnSe₂ single crystals, using in situ high-resolution transmission electron microscopy complemented by first-principles calculations. Lithiation proceeds sequentially through intercalation, conversion, and alloying reactions ($\text{SnSe}_2 \rightarrow \text{Li}_x\text{SnSe}_2 \rightarrow \text{Li}_2\text{Se} + \text{Sn} \rightarrow \text{Li}_2\text{Se} + \text{Li}_{17}\text{Sn}_4$) in a manner that maintains structural and crystallographic integrity, whereas delithiation forms numerous well-aligned SnSe₂ nanodomains via a homogeneous deconversion process, but gradually loses the coherent orientation in subsequent cycling. Furthermore, alloying and dealloying reactions cause dramatic structural reorganization and thereby consequently reduce structural stability and electrochemical cyclability, which implies that deep discharge for Sn chalcogenide electrodes should be avoided. Overall, the findings elucidate atomistic lithiation and delithiation mechanisms in SnSe₂ with potential implications for the broader class of 2D metal chalcogenides.

to meet some of the rapidly growing user needs, especially for large-scale, high power, and energy density applications.^[1] This has prompted continuous development of new electrode materials with novel structures and battery chemistries.^[2,3] Recently, much effort has been devoted to 2D materials as electrodes for LIBs because they can provide layered ionic diffusion channels that are typically larger than the interspacing distance of traditional graphitic materials, to enable fast transport of lithium and other alkaline ions.^[4–6] A wide variety of transition metal dichalcogenides (TMDs) have been explored for the purpose of promising battery electrodes, among which many studies on metal sulfides (MoS₂, WS₂, etc.) have experimentally demonstrated excellent Li-storage capacities that are related to the complex reaction mechanisms consisting of both intercalation and conversion reactions.^[7–11] Noticeably, it is intriguing that tin-based 2D chalcogenides can achieve additional capacity by the Li–Sn alloying process, but this process also makes the phase transitions even more complicated.^[12–25] On the other hand, the lithiation via different pathways may lead

Lithium-ion batteries (LIBs) have been used extensively as essential energy storage technology for consumer electronic devices and electric vehicles. However, their performance remains inadequate


to different intermediate and/or final products, which in turn would strongly affect the reaction reversibility and battery cyclability.^[26–31] Therefore, understanding the phase transformation mechanisms and reaction pathways during lithiation processes is a crucial prerequisite for improving battery performance.

Based on numerous previous studies, it is generally believed that the lithiation of 2D metal sulfides would start from the intercalation of Li ions into the S–S interlayers bonded by the weak van der Waals force. When such intercalation reaches a certain lithium content, it may trigger phase transformations in various forms, such as 2H to 1T phase transition in MoS₂,^[8–11] two-phase or solid-solution-like phase transition in SnS₂,^[16] rocksalt phase disordering in SnS₂,^[17] and metal extrusion in copper sulfides.^[26,27] It turns out that the lithiation of 2D materials may have diverse reaction modalities from one to another, or even within a same material. For this reason, elucidating the lithiation mechanism of each specific type of promising materials is necessary and would be helpful in producing knowledge about the potentially common nature of the underlying electrochemical characteristics of similar TMDs.

Dr. S. Kim, Prof. K. He
Department of Materials Science and Engineering
Clemson University
Clemson, SC 29634, USA
E-mail: kaihe@clemson.edu

Dr. S. Kim, Dr. Z. Yao, Dr. J.-M. Lim, Prof. M. C. Hersam,
Prof. C. Wolverton, Prof. V. P. Dravid, Prof. K. He
Department of Materials Science and Engineering
Northwestern University
Evanston, IL 60208, USA
E-mail: v-dravid@northwestern.edu

Dr. Z. Yao
Department of Chemistry and Chemical Biology
Harvard University
Cambridge, MA 02138, USA

 The ORCID identification number(s) for the author(s) of this article can be found under <https://doi.org/10.1002/adma.201804925>.

DOI: 10.1002/adma.201804925

SnSe₂ has been reported as an outstanding anode material with a high theoretical capacity of 798 mAh g⁻¹, attributed to its full lithium storage from all the intercalation, conversion, and alloying reactions.^[18–25] Compared to SnS₂, SnSe₂ has a relatively larger interlayer spacing of 0.6141 nm, which may lower the diffusion barrier and increase the reversible transport of Li ions.^[19] To date, only a few studies have shown the electrochemical reactivity of SnSe₂ with Li/Na ions, suggesting possible reaction mechanisms based on ex situ X-ray diffraction data.^[19,20] Although these results have provided a general guide of phase evolution during the electrochemical cycling of SnSe₂, the dynamic microstructural changes caused by ionic migration and atomic reorganization, which are essential for battery performance and stability, remain elusive. To address this issue, we aim to dynamically unveil the atomically resolved structural evolution during the entire electrochemical lithiation and delithiation cycles of SnSe₂ using the state-of-the-art in situ transmission electron microscopy (TEM) approach,^[26–32] complemented by the density functional theory (DFT) calculations. The combination of these tools have proven useful for detecting exact electrochemical reaction processes.^[10,17,27,33–35]

Herein, we report the real-time observations of the electrochemical phase transformation of single-crystalline SnSe₂ nanoflakes using in situ high-resolution transmission electron microscopy (HRTEM) and in situ electron diffraction (ED) techniques. We have directly observed three stages of the electrochemical lithiation processes: i) first, the initial intercalation reaction occurs to form the Li_xSnSe₂ (0 < x < 2) phase with expansion of the original 2D crystal lattices and an increase of interlayer spacing in *c*-direction; ii) second, a conversion reaction proceeds via the nucleation and growth of Li₂Se and Sn nanoparticles that remain coherent to the original structure; iii) finally, when deep lithiation (discharge to voltage <0.1 V) is performed, Sn further reacts with Li to form Li₁₇Sn₄ via an alloying reaction. It is worth noting that the electrochemically lithiated products are able to reversibly transform to the original SnSe₂ phase with the highly ordered (001) planes during the delithiation process. With help of DFT calculations, we demonstrate the atomic structures correlated to the reversible phase transformations in SnSe₂ electrode during the electrochemical reactions and elucidate the lithiation and delithiation mechanisms of SnSe₂ electrode.

Single-crystalline SnSe₂ nanoflakes which have the CdI₂-type hexagonal 1T structure were used as an anode material for LIBs. The nanoflakes were prepared using the mechanical exfoliation method,^[36,37] as shown in Figure 1a (details described in the Experimental Section). The mechanically crushed SnSe₂ microparticles were sequentially changed to nanoflakes by a Scotch-tape exfoliation process. The exfoliated nanoflakes were mounted onto a TEM grid (for plan-view observation) or a metal wire (for cross-section view observation) to act as an active electrode, and the Li metal was used as a counter electrode along with the natively coated Li₂O as solid electrolyte for in situ experiments (Figure 1b). The electron diffraction patterns and HRTEM image of the transferred nanoflake indicate that the hexagonal-structured SnSe₂ single-crystal is oriented along the [001]-direction, as shown in Figure 1c–e. First, we conducted in situ lithiation experiments on a vertically mounted nanoflake to visualize the parallel arranged (001) basal planes of SnSe₂

because this cross-section orientation allows for a directly visible structural change upon the intercalation of Li-ion at the beginning of lithiation. Figure 1f shows a TEM image of a pristine SnSe₂ nanoflake contacted to the Li₂O coated Li metal electrode. Li ions move into the layered structure of SnSe₂ under the potentiostatic discharging conditions. The interlayer spacing of (001) planes in the pristine nanoflake is 0.618 nm (Figure 1g), and it is expanded by the inserted Li ions along with gradual transformation into amorphous, as shown in Figure 1h and Movie S1 in the Supporting Information. By precise measurement of the interlayer spacing as a function of lithiation time from the time-lapse HRTEM images (Figure 1i and Figure S1, Supporting Information), we find a continuous change of the interlayer distance with respect to the increasing amount of intercalated Li-ions (x in Li_xSnSe₂). We also note a dramatic increase in the interlayer distance (≈6–8 s, Figure 1j), corresponding to the scenario where the top few layers are peeled off from the edge of the flake, making the distance increase by 8.39% on average (can be 0.708 nm at largest, equivalent to 14.6% expansion in maximum) before amorphization. Later, the electrochemically formed Li_xSnSe₂ changes to an amorphous phase when the Li⁺ intercalation exceeds the critical uptake content (at ≈10 s), indicating that the lithiation starts to change from the intercalation to the conversion. The subsequent conversion phase transformations, associated with the typical nucleation and growth of Li₂Se and Sn phases from an amorphous phase, were also confirmed (Figure S2, Supporting Information).

To clearly identify the full picture of all phase transformations during the lithiation process, especially for those transformations that occur after intercalation, we performed in situ HRTEM observation during the lithiation of SnSe₂ nanoflakes. It is obvious to observe the distinct structure change from the overall contrast difference (TEM images of insets in Figure 2a,e) before and after lithiation, while the HRTEM images (Figure 2a–e) further indicate the formation of a large number of small nanoparticles with a darker contrast embedded in the 2D skeleton upon lithiation. A series of TEM images and the corresponding fast-Fourier transform (FFT) patterns obtained at each lithiation time show that the lattice spacing of the (100) planes gradually increases before changing to an amorphous phase. At an intermediate state where both the structurally expanded Li_xSnSe₂ phase and the pristine SnSe₂ phase coexist (Figure 2b), the (10 $\bar{1}$ 0) reflection in the FFT pattern splits into two spots (Figure 2b inset), indicating that the Li_xSnSe₂ phase expands ≈3.58% but still remains in the same crystal orientation coherently with the pristine SnSe₂ phase. In addition, the formation and propagation of the phase boundary between SnSe₂ and Li_xSnSe₂ were also clearly observed in real time, which is confirmed to follow the two-phase reaction pathway during the intercalation (Figure S3, Supporting Information). Combined with the previous observation of the vertically aligned (001) planes of SnSe₂, we obtained a panoramic view of the first lithiation step—Li ions are inserted into the interlayer opening positions to cause a slight lattice expansion but maintain the integrity of the original 2D framework. Compared to other 2D layered materials, we found that the initial intercalation process of SnSe₂ is similar to the two-phase reaction in SnS₂,^[16] but different from the 2H-1T transition that occurs in MoS₂.^[8–10]

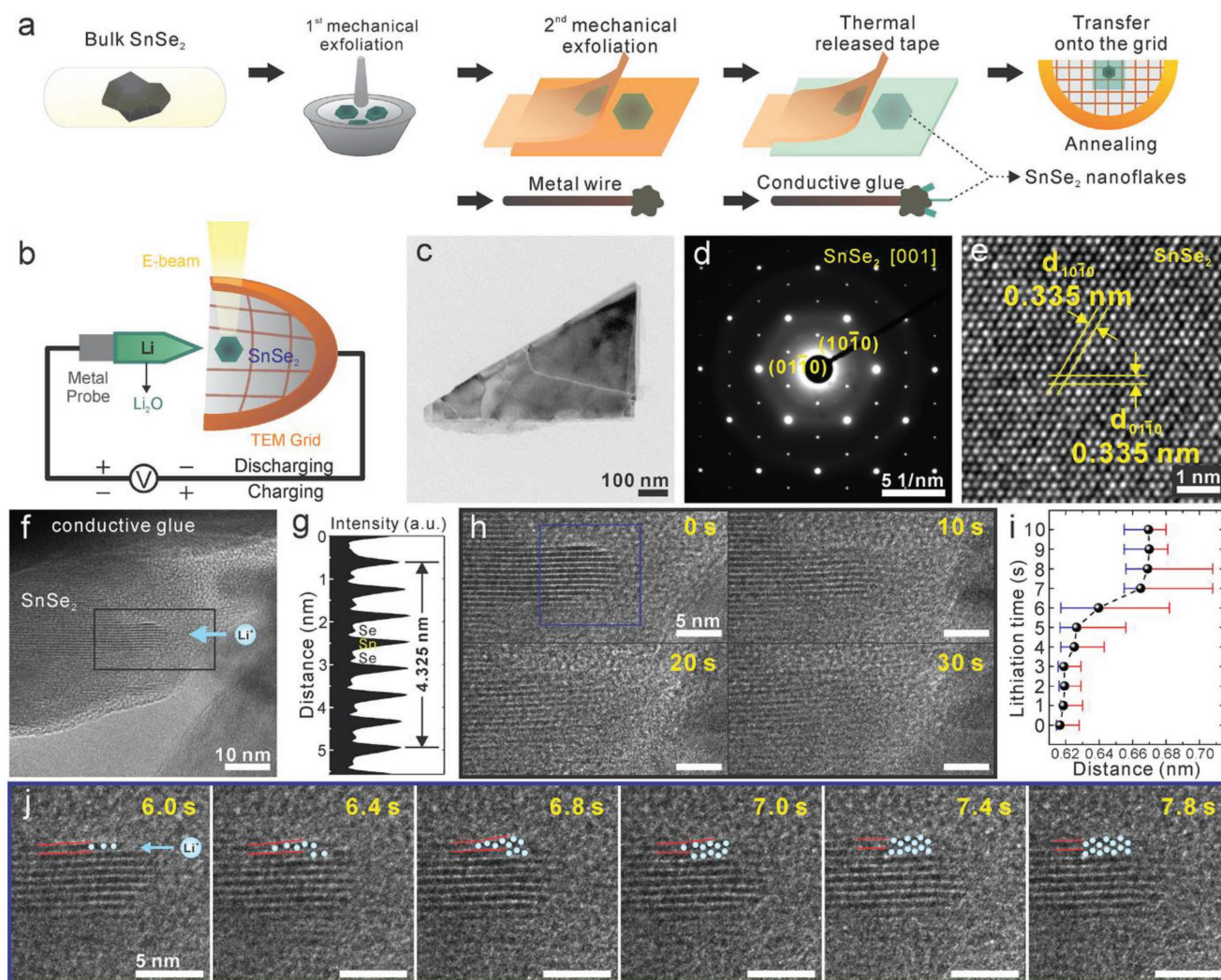
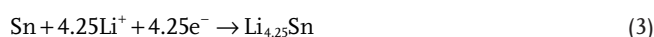
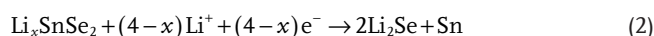


Figure 1. a) Schematic illustration of a single-crystalline SnSe₂ nanoflakes using the mechanical exfoliation method. The in situ TEM samples are mounted onto a half TEM grid and the metal wire to observe phase transformation of SnSe₂ along the planar and cross-section directions, respectively. b) Schematics of in situ TEM experiment setup showing the half-cell battery operated at potentiostatic mode (see details in the Experimental Section). c) TEM image, d) electron diffraction pattern, and e) enlarged HRTEM images of the pristine SnSe₂ nanoflake. f) TEM image showing the electrochemical contact between the vertically mounted SnSe₂ nanoflakes and the Li electrode. g) The interlayer spacing of (001) plane at the pristine state. h) Time-lapse HRTEM images showing phase transformation of SnSe₂ throughout the lithiation process. i) Plot of the interlayer spacing change and j) time-lapse HRTEM images upon Li intercalation but before amorphization (Movie S1, Supporting Information). The red lines and blue circles indicate the bending of SnSe₂ (001) planes and the migration of Li-ions, respectively.

This is because the original 1T structure is preserved during the intercalation process, which suggests a superior structural stability to tolerate the strain induced by Li-intercalation.

With further insertion of Li ions, the structure of Li_xSnSe₂ changes to the amorphous phase (Figure 2c), while the newly formed Li₂Se shows the same orientation as the pristine SnSe₂ nanoflake, indicating that the nucleation and growth of Li₂Se are coherent to the original SnSe₂ structure (Figure 2d). The electrochemically reduced Sn atoms start to agglomerate after insertion of a large amount of Li ions into the matrix and precipitate as Sn nanoparticles (Figure 2e). The Sn precipitation process was found to proceed homogeneously, following a solid-solution-like reaction pathway (Figure S4, Supporting Information). It is worth noting that these Sn nanoparticles would further react with Li and form Li_{4.25}Sn (or Li₁₇Sn₄) alloy

(not shown here but appeared in another lithiation shown in Figure 4b), if a deeper discharge with lower cutoff voltage is performed. The overall lithiation process can store up to 8.25 Li ions per unit cell following the electrochemical reactions shown in Equations (1)–(3)



To confirm the phase transformations identified by in situ HRTEM and FFT analyses, we also performed in situ ED to

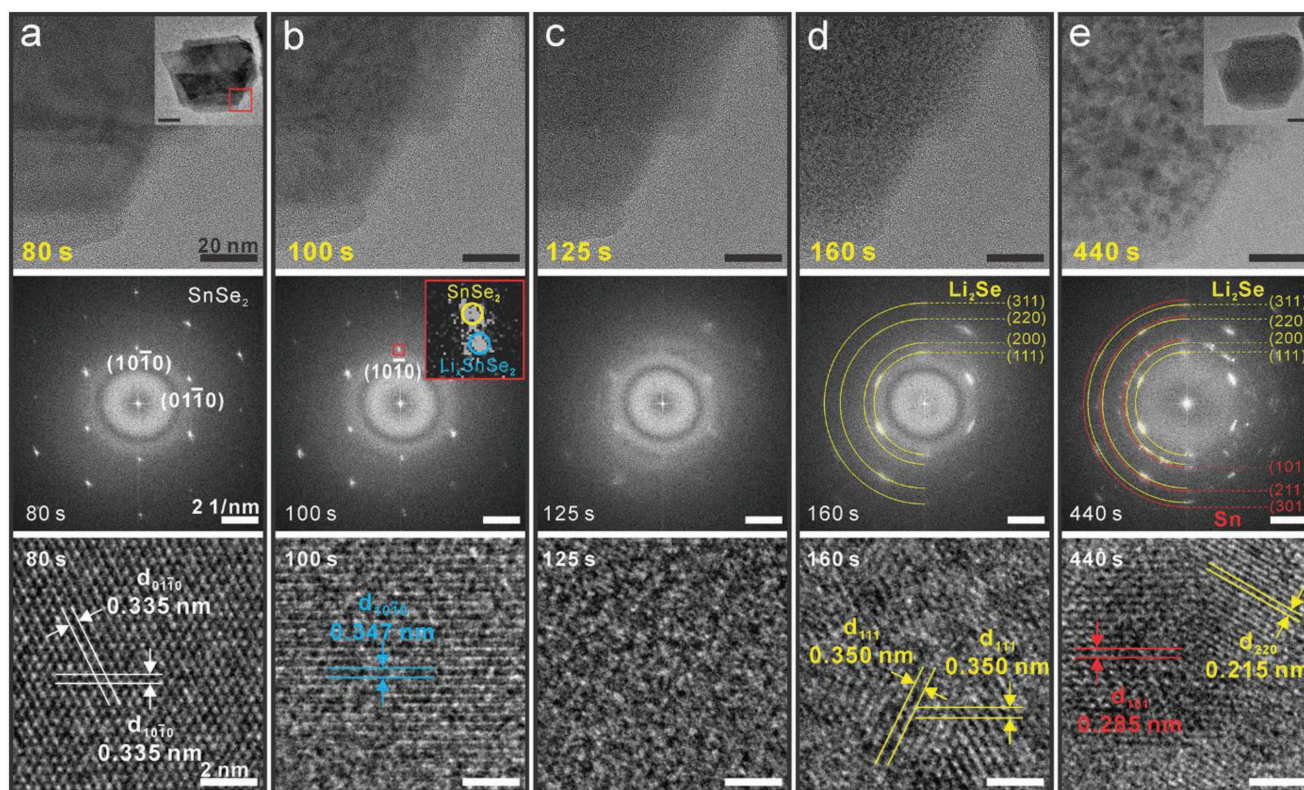


Figure 2. a–e) Time-lapse structural evolution taken at 80 s (a), 100 s (b), 125 s (c), 160 s (d), and 440 s (e), showing representative TEM images (top), FFT patterns (middle), and HRTEM images (bottom) of SnSe₂ nanoflakes during the first lithiation process (Movie S2, Supporting Information). The insets of (a) and (e) show TEM images of the entire nanoflake obtained from the pristine state and the lithiated state, respectively (scale bar: 50 nm). The lattice spacing increases due to the insertion of Li ions, leading to the split of diffraction spot of (10 $\bar{1}$ 0) plane shown in the inset of (b).

monitor real-time phase evolution during lithiation process. The in situ ED patterns sequentially captured from a larger area of a few micrometers collect structural information contributed from more material sampling and thus offer phase identification with higher precision and better statistical validation. **Figure 3** shows ED intensity profile as a function of reaction time during in situ lithiation of SnSe₂, which is derived from radially integrated ED and represented by the false colors. We can clearly observe three stages as Li ions insert into the SnSe₂ lattice, i.e., i) formation of Li_xSnSe₂ phase with lattice expanded (indicated by dashed arrows in Figure 3a); ii) crystal-to-amorphous transition of Li_xSnSe₂ phase with excess Li⁺ intercalation; iii) conversion reaction to form a composite of Li₂Se and Sn. Representative ED patterns captured at each stage (Figure 3b–f) illustrate the coherent crystallography relationship amongst pristine SnSe₂, lithiated Li_xSnSe₂, and converted Li₂Se phases, which is consistent with the FFT analyses shown in Figure 2a–e. Combining both in situ ED and in situ HRTEM results, we now confirm the identical phase transformations during the same lithiation reactions and also validate the reliability of HRTEM and FFT analyses for precise phase identification.

We also investigated the electrochemical phase transformations during the delithiation process because these transformations are critically related to the reversibility and stability of SnSe₂ electrode. We selected another SnSe₂ nanoflake oriented along [001] direction (**Figure 4a**) and completely lithiated it to

the state shown in Figure 4b, in which the FFT pattern indicates the lithiation product is a mixture phase of Li₂Se, Sn, and Li₁₇Sn₄, representing a deep discharge condition after both conversion and alloying reactions. Similar to the previous lithiation, the lithiated phases maintain a well-defined crystal lattice and orientation same to the original host structure. Due to the thermodynamic uphill nature of charging process, the delithiation is not a spontaneous reaction and requires much longer time (3600 s) for the in situ experiments. To minimize the effect of electron radiation, the electron beam was switched to the blank mode during the most delithiation period except for the time to capture images. From the time-lapse HRTEM images and the corresponding FFT patterns shown in Figure 4c–g, we found that most of the lithiated mixture has transformed back to SnSe₂ after the delithiation, which appears as the numerous nanosized domains homogeneously distributed within the original 2D matrix. The enlarged HRTEM image clearly indicates the highly ordered (001) planes of SnSe₂ with a lattice spacing of 0.619 nm after the delithiation for 3600 s, as shown in Figure 4h–l. During the first delithiation cycle, the entire nanoflake remains in a good integrity, mechanically and crystallographically, as evidenced by the well-kept sixfold symmetry in the FFT patterns during the in situ HRTEM imaging. We also conducted control experiments to eliminate the possible effect of electron radiation on SnSe₂ recombination, confirming that the electron beam exposure at the level in our experiments did not affect the electrochemical reactions (Figures S5–S7,

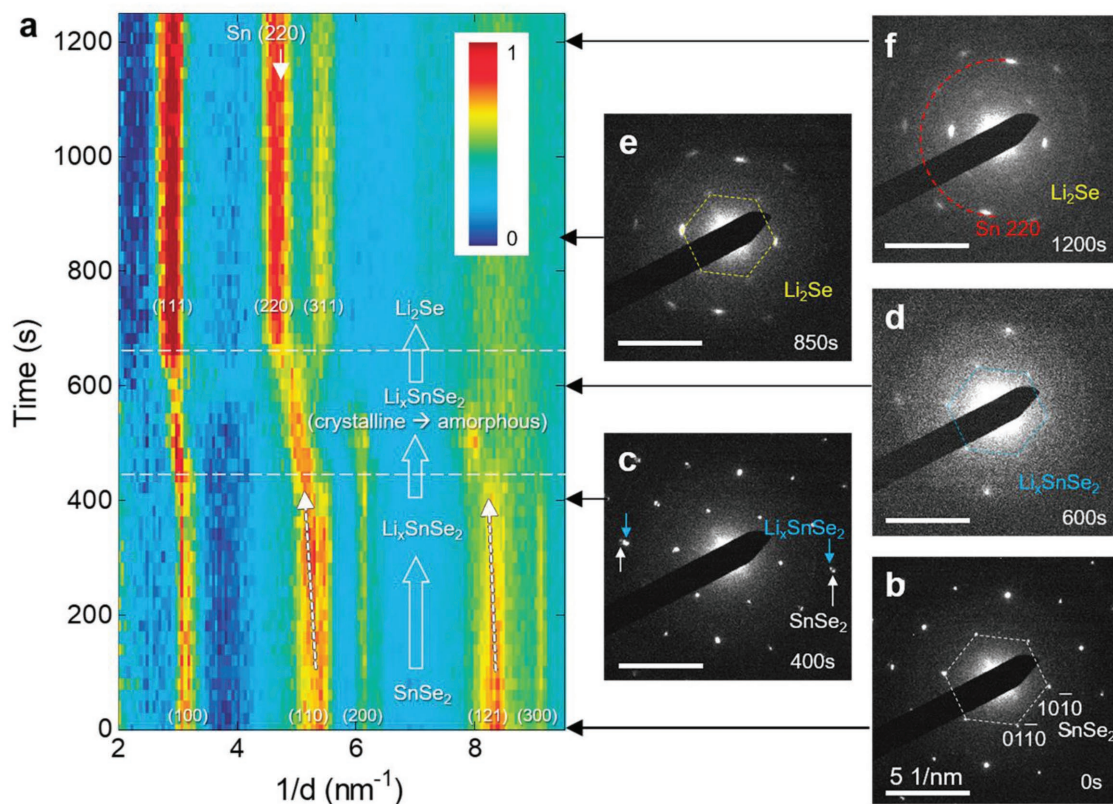


Figure 3. Phase evolution identified by in situ electron diffraction (ED). a) ED intensity profile as a function of time during in situ lithiation of SnSe₂. b–f) Representative ED patterns recorded at various times (Movie S3, Supporting Information).

Supporting Information). Our observation of SnSe₂ recombination provides solid evidence for the reversible deconversion process, which suggests a delithiation mechanism complementary to the previous report.^[19] It is also noted that a certain amount of amorphous phase still exists after the delithiation due to the dramatic volume change caused by the alloying and dealloying of the Li₁₇Sn₄ phase, which is helpful to maintain the flakes in a whole piece by minimizing the volume change along anisotropic directions.^[32] Additionally, the dealloying of Li₁₇Sn₄ takes a long time and overlaps with the deconversion in the timescale during the entire delithiation process. This could leave behind residual Sn and Li due to insufficient time for continued delithiation, and consequently retard the deconversion reaction and/or induce the isolated unusable “dead” Li, which may strongly affect the reversibility of electrochemical cycling. Therefore, we would suggest utilizing only the contributions from the intercalation and conversion reactions and avoiding the alloying reaction, which can largely improve the reversibility and stability even as it compromises the overall capacity.

We continue to monitor the structural evolution of the same nanoflake during the subsequent electrochemical cycling. **Figure 5** shows the HRTEM images indicating the overall change in the second lithiation and delithiation processes. The speckle features in the black–white contrast are associated with the SnSe₂ nanodomains composed of highly ordered (001)-plane stacks, which gradually disappear throughout the lithiation, as shown in the time-lapse HRTEM images in Figure 5a. We managed to control a shallow lithiation without triggering

the alloying process, and thus only Sn and Li₂Se resulting from the conversion reaction were found after the second lithiation, as demonstrated by HRTEM and FFT in Figure 5b–e. Since the second lithiation starts from a polycrystalline nanoflake rather than a single-crystal at the pristine state, a large number of SnSe₂ nanodomains may rotate to more random orientations when Li ions are inserted, and the generated Li₂Se phase does not show the well-defined orientation relationship to the pristine SnSe₂ framework, as evidenced by the more diffusive FFT pattern. After the second delithiation for 3600 s, the majority phase returns back to SnSe₂, while some residual mixture of Li₂Se and Sn still exists without being fully reacted via deconversion (Figure 5f–i). By tracing the same region of SnSe₂ nanoflake, we plot the in-plane area change throughout the first two lithiation/delithiation (discharge/charge) cycles, as shown in Figure 5j. We found that the first cycle was subject to the largest expansion (15.3%) and shrinkage (14%), while the second cycle showed smaller changes (13.9% expansion and 10.2% shrinkage), which may be due to a twofold effect: i) the first cycle involves the extra alloying process not shown in the second cycle; ii) the numerous small SnSe₂ domains in conjunction with the surrounding amorphous phase can buffer more volume change per Li insertion than a single-crystal flake. Nevertheless, these results clearly indicate the electrochemically reversible behavior of SnSe₂ in an LIB.

We conducted DFT calculations to investigate the phase transformation of SnSe₂ through both equilibrium and non-equilibrium lithiation pathways. For the equilibrium pathway,

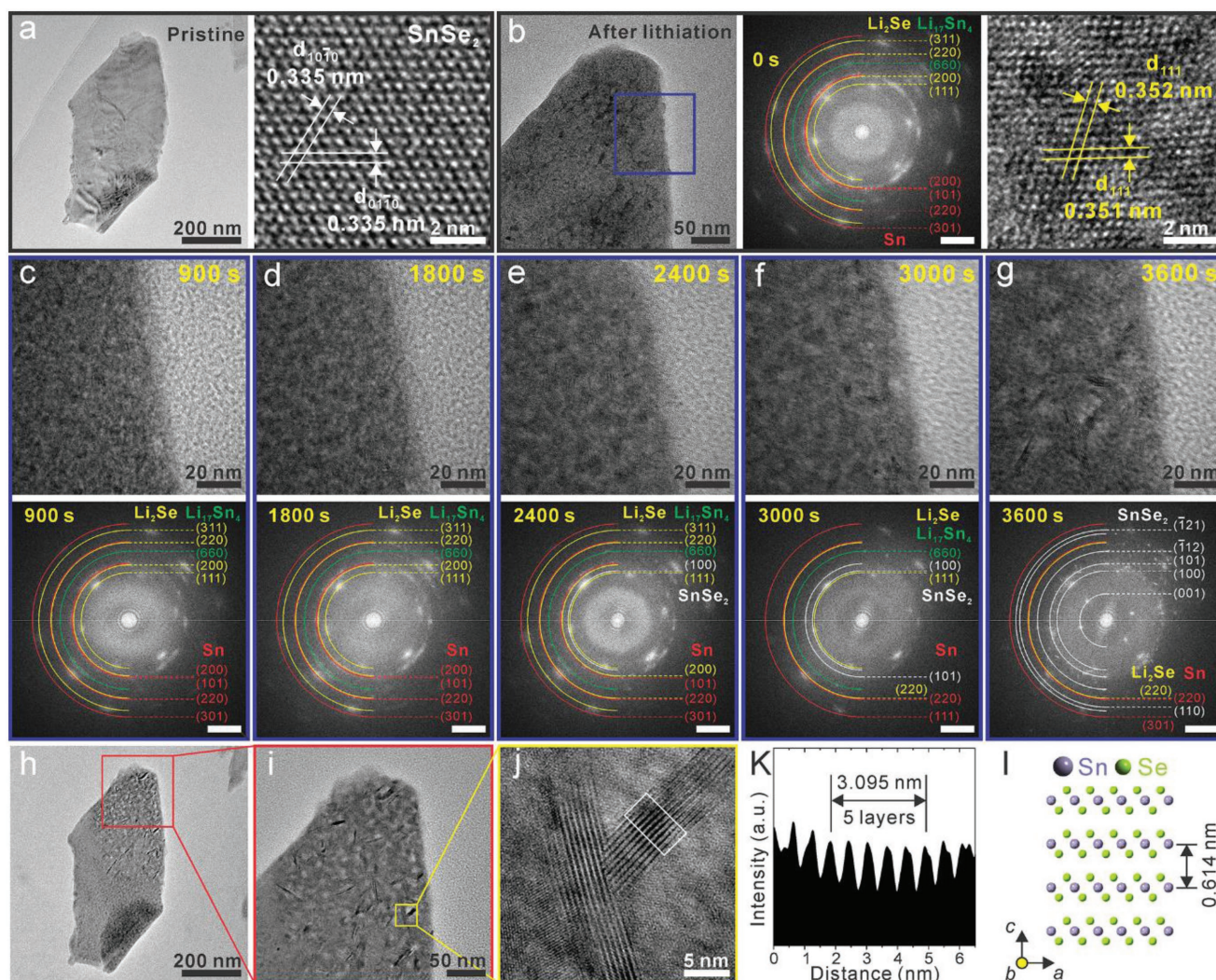


Figure 4. a) TEM images of a [001]-oriented single-crystalline SnSe₂ nanoflake at the pristine state. b) TEM images and FFT pattern (scale bar: 2 nm⁻¹) after the first lithiation showing the mixture of reaction products consisting of Li₂Se, Sn, and Li₇Sn₄. c–g) Time-lapse HRTEM images and the corresponding FFT patterns (scale bar: 2 nm⁻¹) obtained from the blue rectangular region in (b). The beam was blanked except for capturing the images to prevent the radiation damage. h–j) HRTEM images after the first delithiation process showing the formation of numerous small-domain SnSe₂ nanoflakes, with k) interlayer spacing of (001) planes returned to 0.614 nm. l) Atomic structure model of SnSe₂ along [010] direction.

we constructed the Li–Sn–Se ternary phase diagram at 0 K by calculating the formation energies of all the known compounds of the Li–Sn–Se chemical space from the Inorganic Crystal Structure Database^[38] under the framework of the Open Quantum Materials Database.^[39,40] The thermodynamic ground-state Li–SnSe₂ reactions are found to follow conversion (SnSe₂ + 2Li → SnSe + Li₂Se; SnSe₂ + 4Li → Sn + 2Li₂Se) and alloying (Sn → LiSn → Li₃Sn₅ → Li₇Sn₂ → Li₇Sn₄) procedures (Figure S9, Supporting Information), but these $T = 0$ K energetics do not show the intercalation step that has been observed in our present study and previous reports on Li–SnS₂ and Na–SnSe₂ systems.^[16,17] This suggests that the realistic SnSe₂ lithiation experiments proceed in a manner that deviates from ground-state thermodynamic equilibrium. To elucidate the nonequilibrium lithiation pathways, we implemented our recently developed nonequilibrium phase search (NEPS) method (see the Experimental Section)^[32–34] to identify

the structures of intermediate phases from a large number of geometrically distinct Li/vacancy configurations on possible Li-insertion sites of the SnSe₂ structure at different compositions (Li/vacancy ratios). Considering the formation energies in the calculated nonequilibrium Li–SnSe₂ convex hull (Figure S11, Supporting Information), we find that the Li-intercalated Li_xSnSe₂ ($0 < x < 2$) phases are energetically favorable. The pristine SnSe₂ has two types of interstitials, namely octahedral and tetrahedral sites (Figure S10, Supporting Information). Upon lithiation, the Li ions first energetically prefer to occupy the octahedral sites until they are completely filled up ($x = 1$); further Li-ion insertion would occupy the tetrahedral sites and also repel the octahedral Li ions to the nearby tetrahedral site to lower the energy, until all tetrahedral openings are fulfilled ($x = 2$); for further insertion, Li ions would have to be inserted to the octahedral sites again and form a disordered Li–Se compound where all interstitials are occupied ($x = 3$), as

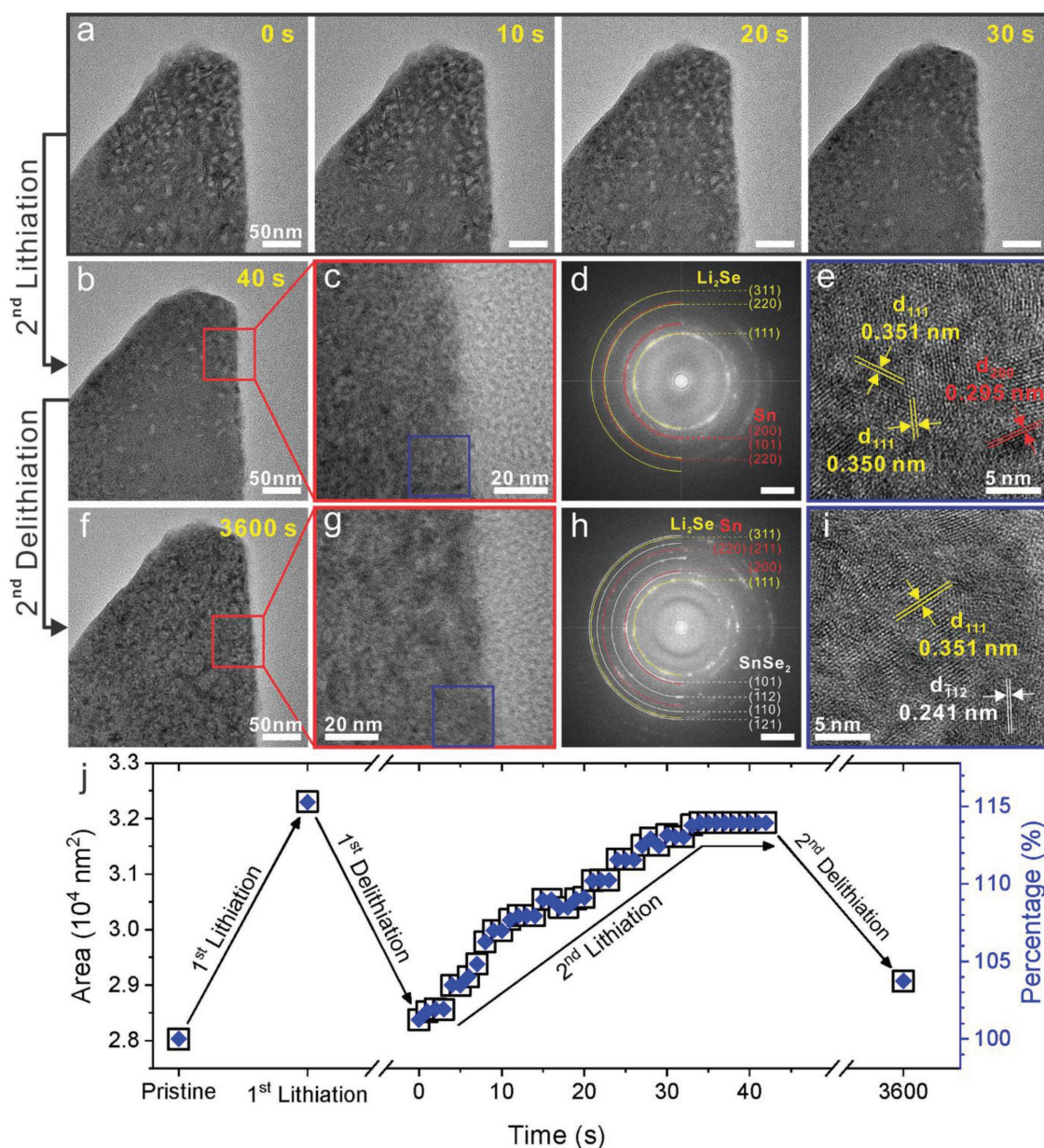


Figure 5. a–f) Time-lapse TEM images during the second lithiation (a,b) (Movie S4, Supporting Information) and delithiation (b–f) cycles. The dark regions in contact with the bright area indicate the highly ordered SnSe₂ phase. c,e) Enlarged HRTEM images and d) FFT patterns (scale bar: 2 nm⁻¹) after the second lithiation process. g,i) Enlarged HRTEM images, and h) FFT patterns (scale bar: 2 nm⁻¹) after the second delithiation process. j) In-plane area change of the SnSe₂ nanoflake as a function of time throughout the first and second electrochemical cycles.

shown in **Figure 6**. It is worth noting that these results are consistent with the experimental observations: SnSe₂ undergoes a Li-intercalation process for $0 < x < 2$ (the first voltage plateau), while further Li-insertion induces an amorphization process when $2 < x < 3$ (the second voltage plateau), which corresponds to the beginning of the conversion reaction; but the overall 2D layered structure maintains high structural integrity for the whole range of $0 < x < 3$, and beyond this point, the original layered crystal lattices collapse and initiate formation of Li₂Se and Sn. This latter step is out of the regime of NEPS method. Nevertheless, the thermodynamic equilibrium calculation can provide key insight into the composition range of $3 < x < 8.25$.

Therefore, we combine the NEPS and ground-state calculations and plot the discharge voltage profile overlaid with the experimental measurement (Figure 6), which shows good agreement.

In summary, we have demonstrated atomic-scale imaging of the reversible phase transformations during the lithiation and delithiation of single-crystalline SnSe₂ nanoflakes in real time. The entire lithiation process involves multiple phase transformation in three stages: 1) the Li intercalation reaction to form the Li_xSnSe₂ ($0 < x < 2$) phase with average 8.39% interlayer expansion and <15% planar expansion; 2) the conversion reaction ($2 < x < 4$) to form structurally coherent Li₂Se and Sn via the nucleation-and-growth pathway; 3) the alloying reaction

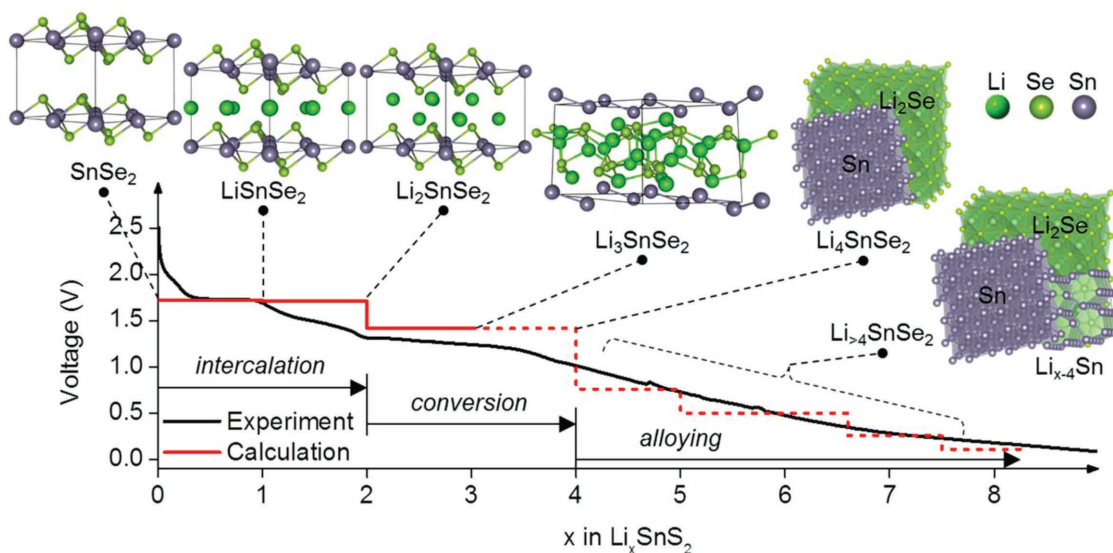


Figure 6. Experimentally measured (black) and DFT calculated (red) discharge voltage profiles along with atomic models corresponding to the predicted intermediate phases during the nonequilibrium ($0 < x < 3$) and equilibrium ($3 < x < 8.25$) lithiation processes in SnSe_2 nanoflakes. The voltage profile corresponding to the intercalation step is predicted using DFT calculation is based on NEPS method (red solid line) and the voltage profiles corresponding to the conversion and alloying steps are calculated using DFT based 0 K thermodynamic equilibrium phase diagram (red dashed line).

($4 < x < 8.25$) to form $\text{Li}_{17}\text{Sn}_4$ under the deep lithiation condition. During the delithiation process, the Li_2Se and Sn can reversibly recombine into numerous well-aligned SnSe_2 nanodomain stacks via a homogeneous deconversion process, but would gradually become crystallographically randomly oriented in the subsequent lithiation/delithiation cycles. We also found that the alloying and dealloying reactions may cause dramatic structural reorganization and consequently reduce the structural stability and electrochemical cyclability; and thus it would be better to avoid deep discharge for Sn based 2D chalcogenides. Combining in situ TEM observation and DFT calculation, the intermediate phases during dynamic lithiation and delithiation cycles have been confirmed and their atomic structure evolution during multiple phase transformations has also been elucidated. Our findings lead to mechanistic understanding of nanoscale (de)lithiation behavior of SnSe_2 and may provide valuable implications to other 2D metal selenides as well as Sn-based chalcogenides.

Experimental Section

Preparation of SnSe_2 Flakes: The [001]-oriented single-crystalline SnSe_2 nanoflakes were prepared using mechanical exfoliation method.^[36,37] The glass tube sealed single-crystalline bulk SnSe_2 flakes were broken down into relatively small and thin flakes in an Ar-filled glove box using a mortar. The fragmented plate with wide dimension was transferred onto a sticky Scotch tape to obtain few-layer SnSe_2 nanoflakes. After repeating the attachment and detachment, the selected SnSe_2 nanoflakes were transferred onto the thermal released tape using the same Scotch tape method. These nanoflakes attached to the thermal released tape were bonded with an ultrathin carbon film supported TEM grid. The Scotch tape was removed during heat treatment without applying physical force to prevent the damage of carbon films. TEM grid was cut with a sharp blade while confirming the location of nanoflakes with an optical microscope. The TEM half-grid was connected to the metal wire

by conductive glue and then mounted onto the in situ TEM holder. The vertically aligned SnSe_2 nanoflakes were picked up from mechanically exfoliated flakes using Cu metal wire and directly mounted onto the TEM holder for in situ experiments.

In Situ TEM Characterization: The Nanofactory TEM-STM holder was used to perform the in situ (de)lithiation in the windowless settings.^[41–44] The nanoflakes loaded on the TEM half-grid or the metal wire were connected to one electrode, and Li metal coated with Li_2O solid electrolyte was connected to the other counter-electrode, which was mounted onto the tip of piezo-driven metal probe in an Ar-filled glovebox. During the in situ electrochemical cycling, a constant negative (discharge) or positive (charge) potential was biased on the active SnSe_2 nanoflakes against the Li anode. The in situ HRTEM imaging was performed on JEOL ARM300CF TEM operated at 300 kV and HRTEM images were recorded using a Gatan OneView-IS camera with full frame size of 4096×4096 pixels. The pixel size of typical HRTEM images is ≈ 0.02 nm, which is sufficient to resolve atomic structures; and the measurement precision of corresponding FFT patterns is limited by the pixel interval of ≈ 0.01 nm⁻¹ in reciprocal space, which ensures the accuracy of phase identification. The constant environment, ultrastable sample stage, and reliable protocol of focusing adjustment ensure the high stability of HRTEM imaging, where any possible artifact information due to sample drifting and defocus has been eliminated as much as possible. Control experiments have been done at pristine, lithiated, and delithiated conditions to demonstrate no obvious radiation damage or electron-beam induced reaction at the electron dose-rate of $100 \text{ e}^- \text{ \AA}^{-2} \text{ s}^{-1}$ (Figures S5–S7, Supporting Information). In situ experiments were performed with electron dose-rate below this value. In situ lithiation and delithiation experiments were reproduced at various locations of multiple samples to ensure the observed phase transformations statistically meaningful.

Electrochemical Measurement: To investigate the electrochemical behavior, the electrode slurry was fabricated by homogeneously mixing with 60 wt% of SnSe_2 active materials, 20 wt% of Super P (Alfa Aesar), and 20 wt% of poly(vinylidene fluoride) binder (Sigma-Aldrich) dissolved in *N*-methyl-2-pyrrolidone (NMP) solution (Sigma-Aldrich), which was cast on Cu foil as a current collector. For the complete evaporation of NMP, the coated slurry was dried overnight at 80°C in vacuum and then pressed uniformly. After punching into a circular shape, 2032 coin-type half cells were assembled with a Celgard 2325 separator, Li foil

as a counter electrode, and 1.0 M LiPF₆ in ethylene carbonate/diethyl carbonate (50/50 vol%), Sigma-Aldrich) as an electrolyte in an Ar-filled glove box. Galvanostatic charge/discharge measurements were carried out with the voltage range from 0.0 to 2.5 V versus Li/Li⁺ at a constant specific current of 50 mA g⁻¹ using Arbin battery test equipment.

First-Principles Calculations: The first-principles DFT calculations reported in this study were conducted via the Vienna ab initio simulation package^[45] with the projector augmented wave potentials^[46] and the exchange-correlation functional of generalized gradient approximation of Perdew–Burke–Ernzerhof.^[47] Two sets of parameters were applied: one for the energy sampling of lower energy configurations and the other for accurate total energy determination of selected structures. For the coarse energy sampling calculations, a plane-wave basis set with a cutoff energy of 300 eV and Γ -centered k-meshes with the density of 2000 k-points per reciprocal atom were used. For the accurate total energy calculations, a plane-wave basis set cutoff energy of 520 eV and Γ -centered k-meshes with the density of 8000 k-points per reciprocal atom. The intermediate phases were searched through the Li–SnSe₂ reaction, using the nonequilibrium phase search method (NEPS)^[33–35] by exploring geometrically distinct Li/vacancy configurations on possible insertion sites of the SnSe₂ structure (Figure S10, Supporting Information) at different compositions (Li/vacancy ratios). The method proceeded as follows: i) identify all possible insertion sites in the original SnSe₂ structure using MINT;^[48] ii) generate all symmetrically distinct configurations with Enum^[49] for a series of compositions Li_x□_{3-x}SnSe₂ (0 < x < 3, where □ denotes a vacancy); iii) sample total energies of all configurations with coarse settings; iv) rank the structures by the total energies for each specific stoichiometry and calculate the formation energies by relaxing three lowest energy structures with accurate settings according to the reaction SnSe₂ + xLi → Li_xSnSe₂; v) construct the lithiation convex hull using the formation energies and determine the composition points on the hull as the nonequilibrium intermediate phases. The average lithiation voltage (relative to Li/Li⁺) was computed using the negative of the reaction free energy per Li added following the ground state convex hull (T = 0 K) to form a series of constant voltage steps along the two-phase regions of the convex hull, which should be viewed as an approximation to the actual voltage profiles.^[50] At elevated temperatures (e.g., room temperature), the abrupt voltage drops become more rounded, due to entropic effects, which would be smoother when finite temperature effects are included.^[51]

Supporting Information

Supporting Information is available from the Wiley Online Library or from the author.

Acknowledgements

This work was partly supported by the Start-up Fund sponsored by Clemson University. This research used resources of the Center for Functional Nanomaterials, which is a U.S. DOE Office of Science Facility, at Brookhaven National Laboratory under Contract No. DE-SC0012704. This work made use of the EPIC facility at Northwestern University's NUANCE Center, which has received support from the Soft and Hybrid Nanotechnology Experimental (SHyNE) Resource (NSF ECCS-1542205); the MRSEC program (NSF DMR-1720139) at the Materials Research Center; the International Institute for Nanotechnology (IIN); the Keck Foundation; and the State of Illinois, through the IIN. This work was supported as part of the Center for Electrochemical Energy Science, an Energy Frontier Research Center funded by the U.S. Department of Energy (DOE), Office of Science, Basic Energy Sciences under Award No. DEAC02-06CH11357. The authors gratefully acknowledge computing resources from: 1) the National Energy Research Scientific Computing Center, a DOE Office of Science User Facility supported by the Office of Science of the U.S. Department of Energy under Contract DE-AC02-

05CH11231; 2) Blues, a high-performance computing cluster operated by the Laboratory Computing Resource Center at Argonne National Laboratory.

Conflict of Interest

The authors declare no conflict of interest.

Keywords

DFT calculations, in situ TEM, lithium-ion batteries, reversible phase transformations, tin selenides

Received: July 31, 2018
Revised: September 21, 2018
Published online:

- [1] J. M. Tarascon, M. Armand, *Nature* **2001**, *414*, 359.
- [2] M. Armand, J. M. Tarascon, *Nature* **2008**, *451*, 652.
- [3] D. Larcher, J. M. Tarascon, *Nat. Chem.* **2015**, *7*, 19.
- [4] E. Pomerantseva, Y. Gogotsi, *Nat. Energy* **2017**, *2*, 17089.
- [5] K. S. Chen, I. Balla, N. S. Luu, M. C. Hersam, *ACS Energy Lett.* **2017**, *2*, 2026.
- [6] M. Pumera, Z. Sofer, A. Ambrosi, *J. Mater. Chem. A* **2014**, *2*, 8981.
- [7] X. Xu, W. Liu, Y. Kim, J. Cho, *Nano Today* **2014**, *9*, 604.
- [8] L. Wang, Z. Xu, W. Wang, X. Bai, *J. Am. Chem. Soc.* **2014**, *136*, 6693.
- [9] P. Gao, L. Wang, Y. Zhang, Y. Huang, K. Liu, *ACS Nano* **2015**, *9*, 11296.
- [10] Q. Li, Z. Yao, J. Wu, S. Mitra, S. Hao, T. S. Sahu, Y. Li, C. Wolverton, V. P. Dravid, *Nano Energy* **2017**, *38*, 342.
- [11] J. Wan, W. Bao, Y. Liu, J. Dai, F. Shen, L. Zhou, X. Cai, D. Urban, Y. Li, K. Jungjohann, M. S. Fuhrer, L. Hu, *Adv. Energy Mater.* **2015**, *5*, 1401742.
- [12] J. W. Seo, J. T. Jang, S. W. Park, C. Kim, B. Park, J. Cheon, *Adv. Mater.* **2008**, *20*, 4269.
- [13] T. J. Kim, C. Kim, D. Son, M. Choi, B. Park, *J. Power Sources* **2007**, *167*, 529.
- [14] I. Lefebvre-Devos, J. Olivier-Fourcade, J. C. Jumas, P. Lavela, *Phys. Rev. B* **2000**, *61*, 3110.
- [15] K. Yin, M. Zhang, Z. D. Hood, J. Pan, Y. S. Meng, M. Chi, *Acc. Chem. Res.* **2017**, *50*, 1513.
- [16] P. Gao, L. Wang, Y.-Y. Zhang, Y. Huang, L. Liao, P. Sutter, K. Liu, D. Yu, E.-G. Wang, *Nano Lett.* **2016**, *16*, 5582.
- [17] S. Hwang, Z. Yao, L. Zhang, M. Fu, K. He, L. Mai, C. Wolverton, D. Su, *ACS Nano* **2018**, *12*, 3638.
- [18] J. Choi, J. Jin, I. G. Jung, J. M. Kim, H. J. Kim, S. U. Son, *Chem. Commun.* **2011**, *47*, 5241.
- [19] D.-H. Lee, C.-M. Park, *ACS Appl. Mater. Interfaces* **2017**, *9*, 15439.
- [20] F. Zhang, C. Xia, J. Zhu, B. Ahmed, H. Liang, D. B. Velusamy, U. Schwingenschlög, H. N. Alshareef, *Adv. Energy Mater.* **2016**, *6*, 1601188.
- [21] Y. Cui, A. Abouimrane, J. Lu, T. Bolin, Y. Ren, W. Weng, C. Sun, V. A. Maroni, S. M. Heald, K. Amine, *J. Am. Chem. Soc.* **2013**, *135*, 8047.
- [22] Z. X. Huang, B. Liu, Z. Kong, Y. Wang, H. Y. Yang, *Energy Storage Mater.* **2018**, *10*, 92.
- [23] Q. Tang, H. Su, Y. Cui, A. P. Baker, Y. Liu, J. Lu, X. Song, H. Zhang, J. Wu, H. Yu, D. Qu, *J. Power Sources* **2018**, *379*, 182.
- [24] A. Gurung, R. Naderi, B. Vaagensmith, G. Varnekar, Z. Zhou, H. Elbohy, Q. Qiao, *Electrochim. Acta* **2016**, *211*, 720.

- [25] C. F. Du, J. R. Li, X. Y. Huang, *RSC Adv.* **2016**, *6*, 9835.
- [26] M. T. McDowell, Z. Lu, K. J. Koski, J. H. Yu, G. Zheng, Y. Cui, *Nano Lett.* **2015**, *15*, 1264.
- [27] K. He, Z. Yao, S. Hwang, N. Li, K. Sun, H. Gan, Y. Du, H. Zhang, C. Wolverton, D. Su, *Nano Lett.* **2017**, *17*, 5726.
- [28] J. Y. Huang, L. Zhong, C. M. Wang, J. P. Sullivan, W. Xu, L. Q. Zhang, S. X. Mao, N. S. Hudak, X. H. Liu, A. Subramanian, H. Fan, L. Qi, A. Kushima, J. Li, *Science* **2010**, *330*, 1515.
- [29] C. M. Wang, W. Xu, J. Liu, J.-G. Zhang, L. V. Saraf, B. W. Arey, D. Choi, Z.-G. Yang, J. Xiao, S. Thevuthasan, D. R. Baer, *Nano Lett.* **2011**, *11*, 1874.
- [30] M. Gu, A. Kushima, Y. Shao, J. G. Zhang, J. Liu, N. D. Browning, J. Li, C. Wang, *Nano Lett.* **2013**, *13*, 5203.
- [31] A. Nie, L. Y. Gan, Y. Cheng, H. Asayesh-Ardakani, Q. Li, C. Dong, R. Tao, F. Mashayek, H. T. Wang, U. Schwingenschlöggl, R. F. Klie, R. Shahbazian-Yassar, *ACS Nano* **2013**, *7*, 6203.
- [32] H. Xie, X. Tan, E. J. Lubber, B. C. Olsen, W. P. Kalisvaart, K. L. Jungjohann, D. Mitlin, J. M. Buriak, *ACS Energy Lett.* **2018**, *3*, 1670.
- [33] Z. Yao, S. Kim, M. Aykol, Q. Li, J. Wu, J. He, C. Wolverton, *Chem. Mater.* **2017**, *29*, 9011.
- [34] M. Amsler, Z. Yao, C. Wolverton, *Chem. Mater.* **2017**, *29*, 9819.
- [35] Z. Yao, S. Kim, J. He, V. I. Hegde, C. Wolverton, *Sci. Adv.* **2018**, *4*, eaao6754.
- [36] J. Kang, D. Shin, S. Bae, B. H. Hong, *Nanoscale* **2012**, *4*, 5527.
- [37] F. Bonaccorso, A. Lombardo, T. Hasan, Z. Sun, L. Colombo, A. C. Ferrari, *Mater. Today* **2012**, *15*, 564.
- [38] A. Belsky, M. Hellenbrandt, V. L. Karen, P. Luksch, *Acta Crystallogr., Sect. B: Struct. Sci.* **2002**, *58*, 364.
- [39] S. Kirklin, J. E. Saal, B. Meredig, A. Thompson, J. W. Doak, M. Aykol, S. Rühl, C. Wolverton, *npj Comput. Mater.* **2015**, *1*, 15010.
- [40] J. E. Saal, S. Kirklin, M. Aykol, B. Meredig, C. Wolverton, *JOM* **2013**, *65*, 1501.
- [41] K. He, S. Zhang, J. Li, X. Yu, Q. Meng, Y. Zhu, E. Hu, K. Sun, H. Yun, X.-Q. Yang, Y. Zhu, H. Gan, Y. Mo, E. A. Stach, C. B. Murray, D. Su, *Nat. Commun.* **2017**, *7*, 11441.
- [42] K. He, H. L. Xin, K. Zhao, X. Yu, D. Nordlund, T. C. Weng, J. Li, Y. Jiang, C. A. Cadigan, R. M. Richards, M. M. Doeff, X.-Q. Yang, E. A. Stach, J. Li, F. Lin, D. Su, *Nano Lett.* **2015**, *15*, 1437.
- [43] K. He, F. Lin, Y. Zhu, X. Yu, J. Li, R. Lin, D. Nordlund, T. C. Weng, R. M. Richards, X.-Q. Yang, M. M. Doeff, E. A. Stach, Y. Mo, H. L. Xin, D. Su, *Nano Lett.* **2015**, *15*, 5755.
- [44] K. He, Y. Zhou, P. Gao, L. Wang, N. Pereira, G. G. Amatucci, K. W. Nam, X.-Q. Yang, Y. Zhu, F. Wang, D. Su, *ACS Nano* **2014**, *8*, 7251.
- [45] G. Kresse, J. Hafner, *Phys. Rev. B* **1993**, *47*, 558.
- [46] P. E. Blochl, *Phys. Rev. B* **1994**, *50*, 17953.
- [47] J. P. Perdew, M. Ernzerhof, K. Burke, *J. Chem. Phys.* **1996**, *105*, 9982.
- [48] K. J. Michel, C. Wolverton, *Comput. Phys. Commun.* **2014**, *185*, 1389.
- [49] G. L. W. Hart, R. W. Forcade, *Phys. Rev. B* **2008**, *77*, 224115.
- [50] M. K. Y. Chan, C. Wolverton, J. P. Greeley, *J. Am. Chem. Soc.* **2012**, *134*, 14362.
- [51] C. Wolverton, A. Zunger, *Phys. Rev. Lett.* **1998**, *81*, 606.